

(De)Sodiation Mechanisms and Cycling Stability of Entropy-Engineered Sodium-Ion Battery Alloy Anodes by Operando X-ray Diffraction

Downloaded from: https://research.chalmers.se, 2026-11-23 17:30 UTC

Citation for the original published paper (version of record):
Dericiler, K., Alvi, S., Persdotter, A. et al (2026). (De)Sodiation Mechanisms and Cycling Stability of Entropy-Engineered Sodium-Ion Battery Alloy
Anodes by Operando X-ray Diffraction. Batteries and Supercaps, 9(11).
http://dx.doi.org/10.1002/batt.70521

N.B. When citing this work, cite the original published paper.

research.chalmers.se offers the possibility of retrieving research publications produced at Chalmers University of Technology. It covers all kind of research output: articles, dissertations, conference papers, reports etc. since 2004. research.chalmers.se is administrated and maintained by Chalmers Library

(article starts on next page)

Check for updates

RESEARCH ARTICLE OPEN ACCESS

(De)Sodiation Mechanisms and Cycling Stability of Entropy-Engineered Sodium-Ion Battery Alloy Anodes by *Operando* X-ray Diffraction

Kuray Dericiler[1,2] | Sajid Alvi[1] | Amanda Persdotter[3] | Valentina Matovic[3] | Samik Roy Moulik[1] | Lorenzo Stievano[4,5,6] | Magnus Hörnqvist Colliander[1] | Patrik Johansson[1,2,6,7]

[1]Department of Physics and Astronomy, Chalmers University of Technology, Göteborg, Sweden | [2]Wallenberg Initiative Material Science for Sustainability, Department of Physics and Astronomy, Chalmers University of Technology, Göteborg, Sweden | [3]Department of Mechanical Engineering, Chalmers University of Technology, Göteborg, Sweden | [4]Réseau sur le Stockage Electrochimique de l'Energie (RS2E), CNRS, Amiens, France | [5]Institut Charles Gerhardt Montpellier (ICGM), Univ. Montpellier, CNRS, ENSCM, Montpellier, France | [6]Alistore-ERI, FR CNRS 3104, Amiens, France | [7]Department of Chemistry – Ångström, Uppsala University, Uppsala, Sweden

Correspondence: Kuray Dericiler (kuray.dericiler@chalmers.se) | Patrik Johansson (patrik.johansson@kemi.uu.se)

Received: 12 June 2026 | **Revised:** 9 October 2026 | **Accepted:** 15 October 2026

Keywords: alloy | anode | chemical engineering | electrolyte | materials science | particle size | synchrotron

ABSTRACT

Alloy anodes represent a high-capacity alternative to the prevalent hard carbon-based anodes for sodium ion-batteries. The major challenge is their large volumetric changes during (de)sodiation, consuming electrolyte and ultimately leading to pulverization of the anode and hence limited cycle life of the battery. To overcome this fundamental challenge, a proof-of-concept solution is introduced in $SnSbBiSe_{1.5}Te_{1.5}$, a high-entropy alloy, as shown by comparing its cycling performance with those of its low-entropy (Sb_2Te_3) and medium-entropy ($SbBiSe_{1.5}Te_{1.5}$) analogs. Using *operando* synchrotron X-ray diffraction, major differences are revealed during the (de)sodiation as function of configurational entropy, and by cross-sectional SEM further insight is gained on the roles of particle size and distribution, both initially and after cycling. Overall, this study highlights the importance of entropy-engineered and controlled particle size alloy anodes to limit volumetric changes and render stable cycling.

1 | Introduction

The ever-growing global energy demand drives the need for efficient energy storage. Lithium-ion batteries (LIBs) are the most widely adopted solution for as diverse needs as mobile devices, electric vehicles, and electricity grids. However, the risk of scarcity of supply and the nonuniform distribution of lithium-containing minerals on Earth's surface are problematic from a long-term sustainability and energy security perspective. Therefore, sodium-ion batteries (SIBs), due to the abundance of sodium and its nonstrategic distribution over the planet, have attracted increasing attention [1]. Despite the many similarities of LIBs and SIBs, there is a need to find better anode materials for SIBs as neither carbonaceous materials, such as soft and most of all hard carbons (HCs) [2], which use insertion/adsorption mechanisms, nor nonmetals and metalloids, such as phosphor [3], silicon [4], and germanium [5], as well as alloys [6], metal oxides [7], and metal chalcogenides [8], using mainly conversion/alloying reactions, have provided the "silver bullet" akin to graphite for LIBs [9]. Carbonaceous materials demand high-temperature synthesis and/or rely heavily on often elaborate and expensive chemical modifications [10], while alloy anodes, with very high theoretical capacities, undergo large volumetric expansions and contractions during sodiation and desodiation, respectively, resulting in an unstable solid electrolyte interphase (SEI) leading to poor cycling stability and ultimately pulverization

Kuray Dericiler and Sajid Alvi contributed equally to this work.

This is an open access article under the terms of the Creative Commons Attribution License, which permits use, distribution and reproduction in any medium, provided the original work is properly cited.

© 2026 The Author(s). *Batteries & Supercaps* published by Wiley-VCH GmbH.

of the anode [11]. Furthermore, alloys are also restricted by their electrical conductivity, resulting in both low specific capacity due to the need to incorporate large amounts of conductive additives to the anode and limited rate capability [12, 13].

High-entropy alloys (HEAs), based on solid-solution and entropy stabilization [14–16], and combining conversion/alloying reactions, in principle offer unique advantages; the initial conversion reaction can produce an inert matrix that effectively buffers the volume change resulting from the subsequent alloying reaction. Binary [17–19] and ternary [20, 21] alloys, as well as their composites [22, 23], have been studied extensively to understand the underlying storage mechanisms and to realize the full potential of their high sodium storage capacity. Moving further, entropy was recently shown to play a positive role in the cycling stability of medium-entropy alloy (MEA) anodes applied to LIBs [24, 25].

Here, HEAs are applied to SIBs by introducing the proof-of-concept solution $SnSbBiSe_{1.5}Te_{1.5}$. The main hypothesis is that the combination of conversion and alloying elements and mechanisms contributes to the overall capacity while maintaining a conductive network [26, 27]. To prove this hypothesis, the electrochemical performance of alloys with different configurational entropy is evaluated first; Sb_2Te_3, a low-entropy alloy (LEA), $SbBiSe_{1.5}Te_{1.5}$, an MEA, and $SnSbBiSe_{1.5}Te_{1.5}$, synthesized by one-step and two-step (second step with isopropyl alcohol) ball milling (BM), named HEA and HEA-IPA, respectively. Furthermore, *operando* synchrotron X-ray diffraction (SXRD) is employed to elucidate the (de)sodiation mechanisms and the nature of the (de)sodiated phases. Finally, the impact of initial particle size and distribution, as well as their evolution, on the cycling stability is revealed by cross-sectional SEM coupled with analysis building on convoluted neural networks (CNNs).

2 | Experimental Section

2.1 | Synthesis of LEAs, MEAs, and HEAs

Bi (45 µm, 99.5%) and Sb (45 µm, 99.5%) powders were purchased from GoodFellow Cambridge Ltd. (Huntingdon, England), Se (45 µm, 99.999%) powder was purchased from Thermo Fisher Scientific (MI, USA), Te (75 µm, 99.99%) and Sn (10 µm, 99.95%) powders were purchased from US Research Nanomaterials Inc. (Houston, TX, USA). For the $SnBiSbSe_{1.5}Te_{1.5}$ HEA synthesis, stoichiometric amounts of Sn, Bi, Sb, Se, and Te were subjected to BM using a 45 ml zirconia jar and zirconia balls (5 mm ∅) with a ball-to-powder ratio of 20:1. The BM was carried out in two steps: the first step under an Ar atmosphere for 61 h with alternate 10 min BM at 600 rpm and 30 min cooling stages, and the second step in an isopropyl alcohol (IPA, ≥99.9%, VWR International, France) medium for 1 h with 10 min BM at 600 rpm and 30 min cooling stages. All BM were carried out on a high-energy planetary ball mill (Pulverisette 7 Premium line, Fritsch, Germany). BM in IPA was performed to reduce the average particle size and narrow the size distribution [28].

For comparison, an MEA, $BiSbSe_{1.5}Te_{1.5}$, and an LEA, Sb_2Te_3, were synthesized using stoichiometric amounts of Bi, Sb, Se, and Te using the same BM procedure, without employing the IPA medium step. The configurational entropy for each alloy was calculated assuming random mixing on a single lattice from the elemental composition acquired by the EDX analysis (Table S1). Before electrode fabrication, all powders were handled in an Ar-filled glovebox to avoid oxidation in ambient air.

2.2 | Electrode Fabrication and Coin Cell Assembly

HEA-IPA electrodes were prepared by mixing the active material (AM, 70 wt%) with Super P carbon (20 wt%, Alfa Aesar, Germany), sodium carboxymethyl cellulose (CMC, 5 wt%, Sigma–Aldrich, USA), and styrene butadiene rubber (SBR, 5 wt%, Electrodesandmore, USA) in deionized water. The slurry was subsequently cast onto an aluminum foil (17 µm, Schlenk Metallfolien GmbH & Co. KG, Germany) and dried at 80 °C in a vacuum oven for 12 h. Electrodes (13 mm ∅) were cut out and further dried in vacuo at 80 °C for 12 h. The mass loading of active material in the electrode was kept between 1.5 and 2.0 mg/cm^2 and coating thickness of ca. 16 µm. The same procedure was also employed to prepare the HEA, MEA, and LEA electrodes.

Free-standing (FS) electrodes were prepared by mixing AM (70 wt%), Super P carbon (25 wt%), and polytetrafluoroethylene (PTFE, 5 wt%, Sigma–Aldrich, USA) in a mortar. A small amount of IPA was added and the resulting slurry continuously stirred until the IPA had fully evaporated, yielding a dough-like product which subsequently was spread on a glass substrate and vacuum-dried at 70–80 °C for 24 h. Finally, 4 mm electrode disks were cut containing 2–6 mg of AM (15.9–47.7 mg/cm^2). The FS electrodes were used for ex situ SXRD to improve signal quality by eliminating the reflections from the current collector and maximizing transmission.

Coin cells (CR2032) were assembled in an Ar-filled glovebox using sodium metal (0.2 mm thickness, 12 mm ∅, purity >99.8%, Honjo Metals) as negative electrode, a glass fiber separator (420 µm thickness, Whatman GF/C, GE Healthcare), and a 1.0 M solution of $NaPF_6$ in ethylene carbonate (EC) and diethyl carbonate (DEC) (50:50 vol%) with 5 wt% fluorinated EC (FEC) electrolyte (90 µL, E-lyte Innovations GmbH, Münster, Germany) as the electrolyte.

2.3 | Characterization

The as-synthesized HEA, MEA, and LEA powders were characterized using a Bruker D8 Discover X-ray diffractometer (MA, US) equipped with the Cu Kα radiation ($\lambda = 1.54$ Å). Powder morphology and compositional analysis were carried out using scanning electron microscopy (SEM, Zeiss Ultra 55, Germany, and JEOL JSM-7800F Prime, Japan) equipped with energy-dispersive X-ray spectroscopy (EDX) and an accelerating voltage and working distance of 15 kV and 10 mm, respectively. The particle size distribution analysis was carried out using software ImageJ [29] (Table S2).

Galvanostatic cycling (GC) discharge/charge was performed using half-cells in the potential range 0.01–2.00 V versus $Na^+/Na°$ at C/5 rate at room temperature (22 °C) and a battery test system (Scribner 585, NC, USA). The differential capacity (dQ/dV) plots were smoothed using an adjacent averaging algorithm using OriginPro 2023 (Academic) to improve the visual quality. Raw

25666223, 2026, 11, Downloaded from https://chemistry-europe.onlinelibrary.wiley.com/doi/10.1002/batt.70521 by Chalmers University Of Technology, Wiley Online Library on [10/11/2026]. See the Terms and Conditions (https://onlinelibrary.wiley.com/terms-and-conditions) on Wiley Online Library for rules of use; OA articles are governed by the applicable Creative Commons License

plots (without smoothing) are provided in the Figure S3. All potentials are given versus $Na^+/Na°$.

Operando SXRD in transmission geometry was conducted at the DanMAX beamline of the MAX IV synchrotron facility in Lund, Sweden. The X-ray beam size was $711 \times 640\,\mu m^2$ with an energy of 35 keV ($\lambda = 0.354$ Å). The area detector (DECTRIS PILATUS3 X 2M CdTe, grid 1679 × 1475 pixels, pixel size 172 µm) with a sample-to-detector distance of 400 mm was used to collect the Debye ring patterns with 3 s exposure time every 68 s. Two different electrochemical cells were used; hexagonal cells, designed at LRCS, France, with Be windows [30], and AMPIX cells, designed at Argonne National Laboratory, USA, with glassy carbon windows [31]. GC was performed using both cells and the very same half-cells, protocol, and temperature as the in-house experiments, but using another battery test system (Biologic VMP3, France). Ex situ SXRD analysis was conducted on MEA, HEA, and HEA-IPA powders as well as FS MEA and HEA electrodes at different sodiation levels.

The particle size distribution and morphology of selected electrodes were analyzed in cross-section by SEM after 0, 5, and 30 cycles in the desodiated state. The instruments used were a FEI Quanta ESEM 200, operated in high vacuum mode, and a Zeiss Ultra 55 FEG SEM, both equipped with a field emission gun. The SEMs were operated at accelerating voltages of 10 keV for back-scattered electron (BSE) imaging in the former and 0.5 keV for the higher-resolution images from the latter. Both secondary electrons (SEs) and BSEs were used for imaging. The wide cross sections were prepared by broad ion beam (BIB) milling in a Hitachi ArBlade5000 equipped with an Ar-ion gun, operated at 6 kV, with 30° stage swing motion (to reduce curtaining artifacts) and an active intermittent beam setting (beam on 1 s + beam off 1 s), to allow for heat dissipation during ion milling. Prior to milling, the electrodes were cut in half by scissors and glued with Loctite 415 onto an Al substrate for easier subsequent handling.

Particle analysis was performed on the cross-sectional SEM images of LEA-, HEA-, and HEA-IPA-based electrodes: pristine, after 5 cycles, and after 30 cycles, thus 9 samples in total, by segmenting the images using CNN with the UNet architecture [32–35] (Figure S20). The training approach and metrics confirm tight alignment between training and validation for each model (Figures S21 and S22). The number of particles in each size interval was normalized to the total analyzed area of each sample, yielding a frequency distribution which allows cross-sample comparisons of particle sizes.

3 | Results and Discussion

In this section, first the structure and morphology of as-synthesized HEA-IPA and HEA are outlined. Second, the electrochemical half-cell performance is reported and discussed upon, followed by *operando* SXRD data analysis of the structural evolution during (de)sodiation. Finally, the cross-sectional SEM analysis of particle data using CNNs is provided.

3.1 | Structure and Morphology

The SXRD pattern of the HEA shows a phase-pure composition consisting of reflections from only a single trigonal crystal structure (Figure 1a) within the rhombohedral $R\bar{3}mH$ space

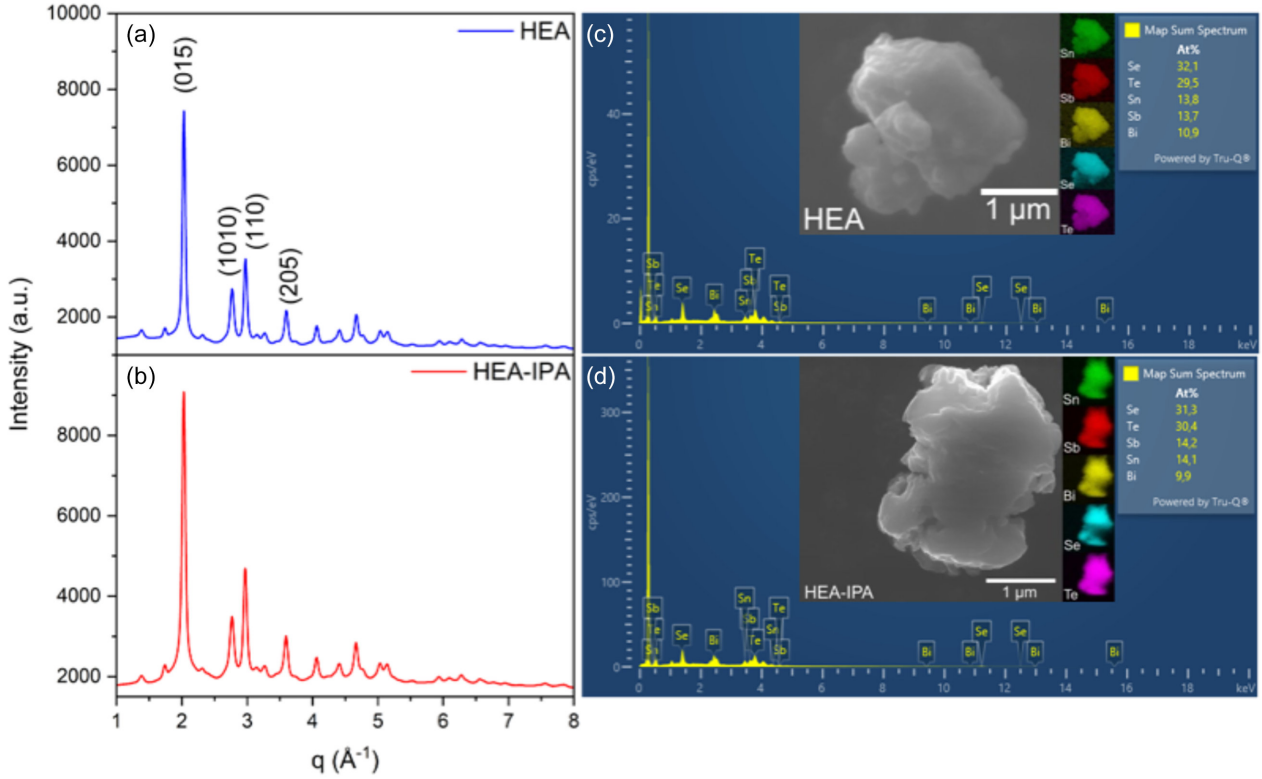


FIGURE 1 | SXRD patterns (a,b) and EDX analysis (c,d, insets: SEM images of the analyzed particles) of HEA and HEA-IPA, respectively.

25666223, 2026, 11, Downloaded from https://chemistry-europe.onlinelibrary.wiley.com/doi/10.1002/batt.70521 by Chalmers University Of Technology, Wiley Online Library on [10/11/2026]. See the Terms and Conditions (https://onlinelibrary.wiley.com/terms-and-conditions) on Wiley Online Library for rules of use; OA articles are governed by the applicable Creative Commons License

group. The pattern of the HEA-IPA sample indicates that BM with IPA does not modify the structure of the HEA nor lead to any phase separation (Figure 1b). The SEM-EDX analysis of HEA reveals a homogenous elemental distribution within the particle (Figure 1c) and flake-like morphology (Figure 1c, inset), HEA-IPA showing the same morphology and elemental distribution (Figure 1d). The XRD patterns of LEA and MEA indicate the same single-phase trigonal structure within the rhombohedral $R\bar{3}mH$ space group as HEA and HEA-IPA (Figure S1a,b), while the SEM-EDX analyses confirm the elemental composition and display flake-like particle morphology (Figure S1c,d). The overview SEM micrographs (Figure S2) show that as-synthesized alloy powders have similar particle morphologies and indicate a significant reduction in the average particle size on going from HEA to HEA-IPA (Figure S2c,d, respectively).

3.2 | Electrochemical Performance

GC clearly shows the effect of entropy stabilization along the series of LEA-, MEA-, and HEA-based anodes; the former shows significant degradation after a mere 5 cycles, while the latter shows slightly higher cycling stability after 30 cycles (Figure 2a). HEA-IPA shows a slightly lower initial capacity (~327 mAh/g) as compared to MEA and HEA (~400 mAh/g), but also a more stable cycling. This is due to the micron-sized particles of HEA which initially benefit from a reduced specific surface area, consuming less electrolyte during the SEI formation stage and hence delivers higher initial capacity. However, extreme volume variations trigger in situ pulverization and mechanical cracking of these microparticles, causing their performance to drop and subsequently match the submicron particles (HEA-IPA) by the 30th cycle. In contrast, the submicron particles, which do suffer from a lower initial Coulombic efficiency (CE) and lower capacity due to extensive SEI formation on their large surface areas, successfully suppress particle fracturing, resulting in vastly improved cycling stability [36].

Cycling stability tracked by monitoring the CE shows the MEA-, HEA-, and HEA-IPA-based cells to all initially be at ~99% CE, but for the two former ones, it varies slightly after 30 cycles (Figure 2b). This is possibly due to expansion-induced crack formation, creating a larger surface area, resulting in a thinner and less stable SEI. Consequently, both the reduced particle size and the higher configurational entropy contribute to improved cycling stability.

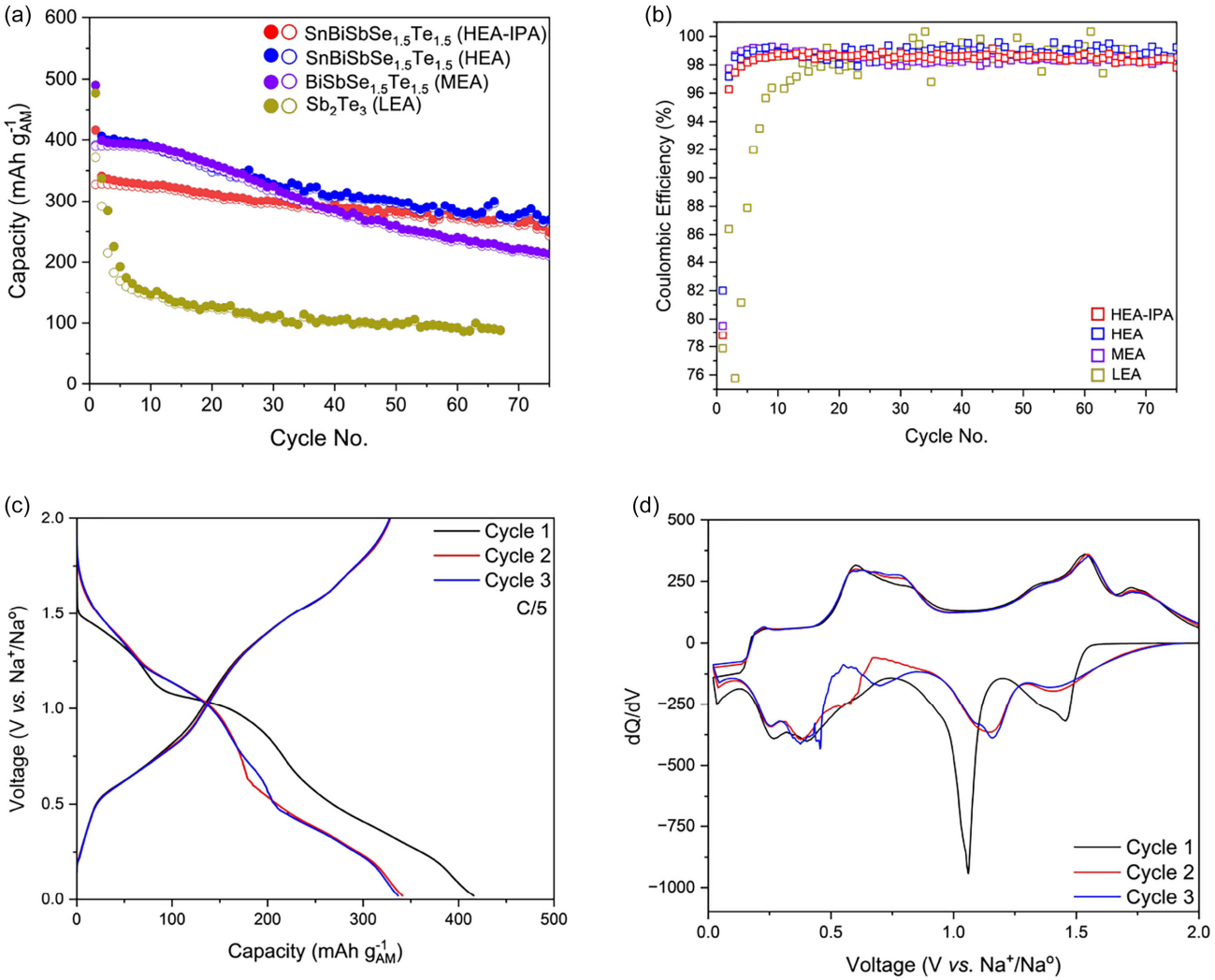


FIGURE 2 | GC (a) and CE (b) of LEA-, MEA-, HEA-, and HEA-IPA-based cells, charge–discharge curves (c), and dQ/dV plots (d) of HEA-IPA initial cycles.

25666223, 2026, 11, Downloaded from https://chemistry-europe.onlinelibrary.wiley.com/doi/10.1002/batt.70521 by Chalmers University Of Technology, Wiley Online Library on [10/11/2026]. See the Terms and Conditions (https://onlinelibrary.wiley.com/terms-and-conditions) on Wiley Online Library for rules of use; OA articles are governed by the applicable Creative Commons License

The charge–discharge curves of the HEA-IPA-based cell exhibit three plateaus (Figure 2c) and the dQ/dV plots (Figure 2d) display the corresponding reactions' positions. Initially, during sodiation, between 1.56 and 1.21 V, electrolyte decomposition and SEI formation possibly accompanied by Na^+ intercalation are observed. The latter process was previously reported for $Bi_{0.25}Sb_{1.75}Te_3$ using a similar electrolyte, albeit at a slightly lower potential (0.93 V) [23]. This is followed by a stronger and broader feature in the range of 1.19–0.73 V, associated with Na^+ reactions with selenides [37] and tellurides [22]. Subsequently, alloying reactions with Bi [22] and Sb [23] at 0.40 V and with Sn [21] at 0.26 V were observed. The subsequent sodiation cycles display slight variations in the potentials; the conversion at 1.06 V shifts to *ca*. 1.13 V during the second cycle, and eventually decomposes into two distinct features at 1.08 and 1.15 V. This potential shift after the first cycle has previously been attributed to restructuring and reduction of particle size of the AM [17, 38], while the variations have been attributed to structural relaxations or induced stress due to formation of intermediary structures and/or to the structure of the alloy itself [23, 39]. Additionally, the peak associated with electrolyte decomposition, SEI formation, and intercalation reduces in intensity due to the irreversibility of the former reaction, but its presence possibly indicates active intercalation.

In contrast to the sodiation reaction potentials, the desodiation reaction potentials are more consistent with five peaks at 0.59, 0.78, 1.34, 1.54, and 1.72 V. While the broad and partly overlapping peaks make any assignment ambiguous, these have previously been attributed to Sn [20], Bi [40], and SnSb [41] (0.6 V), Sb [20] and Bi [40] (0.78 V), Te [42] (1.46 V), and finally, Se [43] (1.52 and 1.77 V).

For the charge–discharge curves of the LEA-, MEA-, and HEA-based cells (Figure S4a–c, respectively), a similar initial sodiation behavior is observed, with several plateaus at 1.1 and 0.6 V. In addition, the LEA-based cell shows a capacity contribution below 0.2 V, but with a rapid capacity fading during desodiation, due to inefficient sodium extraction below 1.5 V (Figure S4a). The following cycles confirm the capacity contribution from the plateau at 0.05 V for LEA, but this only lasts for a few cycles. Looking at the MEA and HEA data, these cells display more similar behavior to the HEA-IPA-based cell (above), with the only major difference being the absence of any capacity contribution from the plateau between 1.5 and 1.2 V for the former (Figure S4b).

3.3 | Structural Evolution During (De)Sodiation

The structural changes in MEA upon (de)sodiation are studied first, this as this material is a relatively simpler system as compared to the HEA. The *operando* SXRD patterns collected using the AMPIX cell (Figure 3a) and a magnified view of the regions of interest (Figure 3b) indicate that, during the early

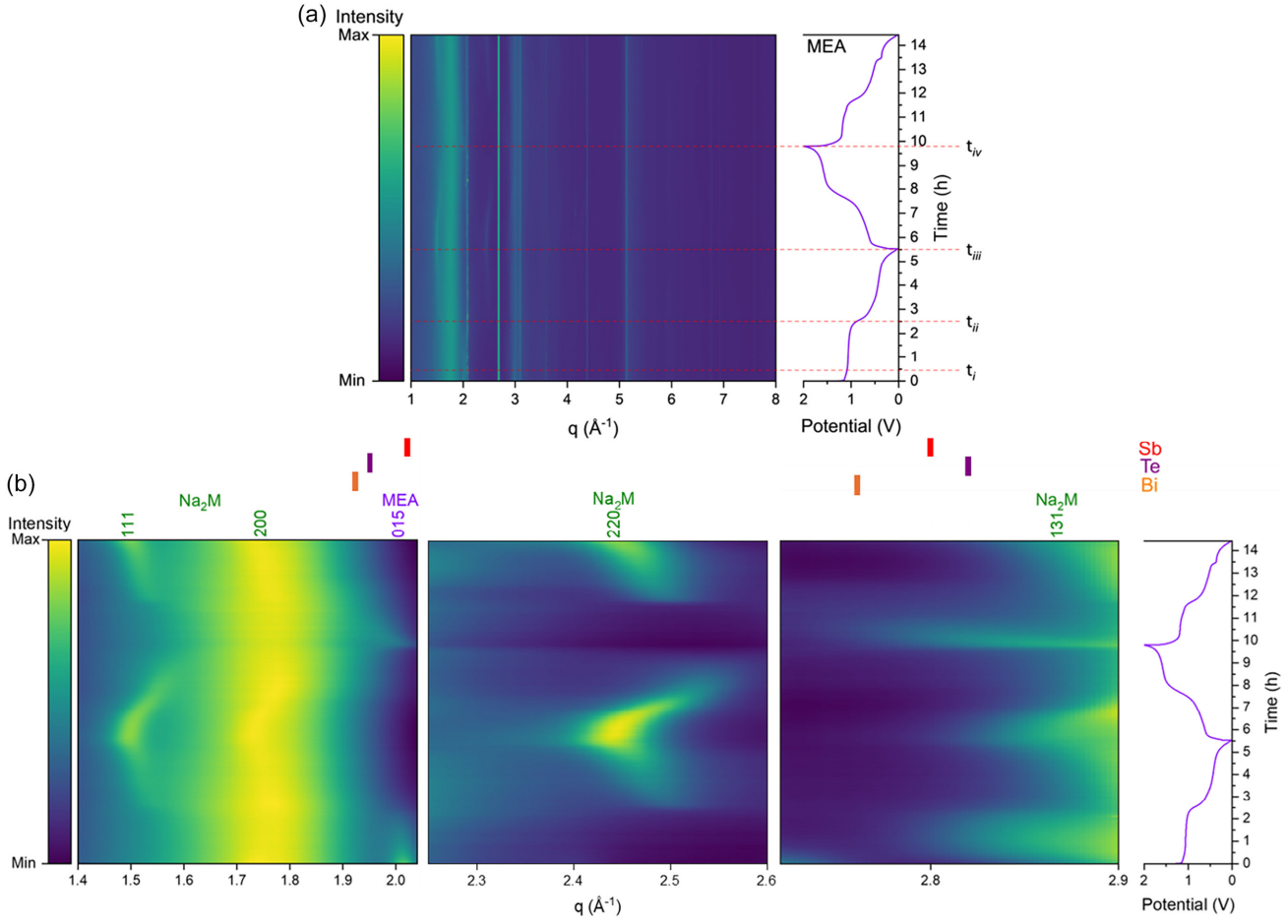


FIGURE 3 | Overall *operando* SXRD pattern of MEA (a) and specific regions of interest (b).

25666223, 2026, 11, Downloaded from https://chemistry-europe.onlinelibrary.wiley.com/doi/10.1002/batt.70521 by Chalmers University Of Technology, Wiley Online Library on [10/11/2026]. See the Terms and Conditions (https://onlinelibrary.wiley.com/terms-and-conditions) on Wiley Online Library for rules of use; OA articles are governed by the applicable Creative Commons License

stages of sodiation and throughout the first plateau (between t_i and t_{ii}) a phase separation occurs, leading to the formation of partially sodiated $Na_2(TeSe_3)$ (Figure S5), which crystallizes within the monoclinic $C12/c1$ space group (ICSD #63011). The absence of reflections matching Bi, Sb, or Te structures (Figure 3b) together with the increase in the background signal of the normalized SXRD patterns (Figure S7) suggest the formation of additional amorphous species, as the overall composition should be preserved. At the end of the first plateau (t_{ii}), highly sodiated Na_2Te, that is, the most sodiated Te phase crystallizing within the cubic $Fm\bar{3}m$ space group (ICSD #60437), forms. The sodiation then continues, via Sb and Bi storing additional sodium through the formation of Na_xSb and Na_yBi, the interplanar spacing increases and this structure is henceforth named Na_zM ($2 < z < 3$, M = Se, Te, Sb, and Bi). This becomes the dominant phase in which sodium is stored at high sodiation levels (t_{iii}). The ex situ SXRD pattern of the fully sodiated FS MEA electrode and the XRD pattern of cubic Na_2Te (ICSD) (Figure S6) together prove that the structure remains cubic in its fully sodiated state, while no hexagonal Na_3Sb and Na_3Bi phases are observed. A cubic polymorph of Na_3Sb has previously been observed during electrochemical sodiation of pure Sb [44]. While this polymorph is expected to form only at pressures >1.3 GPa [45], it is more stable than the hexagonal polymorph [46]. The absence of hexagonal Na_3Sb and Na_3Bi can be explained either by the activation barrier of the phase transformation simply is too high to be overcome by the chemical potential change by additional Na or, as suggested by the ex situ SXRD patterns, the additional Na is stored as amorphous species.

During charge, as sodium is extracted from Na_zM, the interplanar spacing decreases, and eventually the Na_2Te structure is recovered (Figure 3). As the desodiation continues, the interplanar distances continue to decrease before the loss of the long-range ordering, indicating the amorphization of the material. At the fully desodiated state (t_{iv}), a phase separation is observed similar to the structure between t_i and t_{ii}, revealing that the loss of the initial MEA structure happens as early as the first stages of sodiation, and this multi-phase "transformed" structure must remain the main electrochemically active component (Figure 3). Any subsequent sodiation is identical to the initial sodiation of MEA, with the exception being that the phase segregation has already occurred.

The *operando* SXRD data for MEA using the hexagonal cell confirm the findings obtained using the AMPIX cell; both with regards to the "transformed" and Na_2M phases as well as the changes in the lattice spacing (Figures S8 and S9)—also

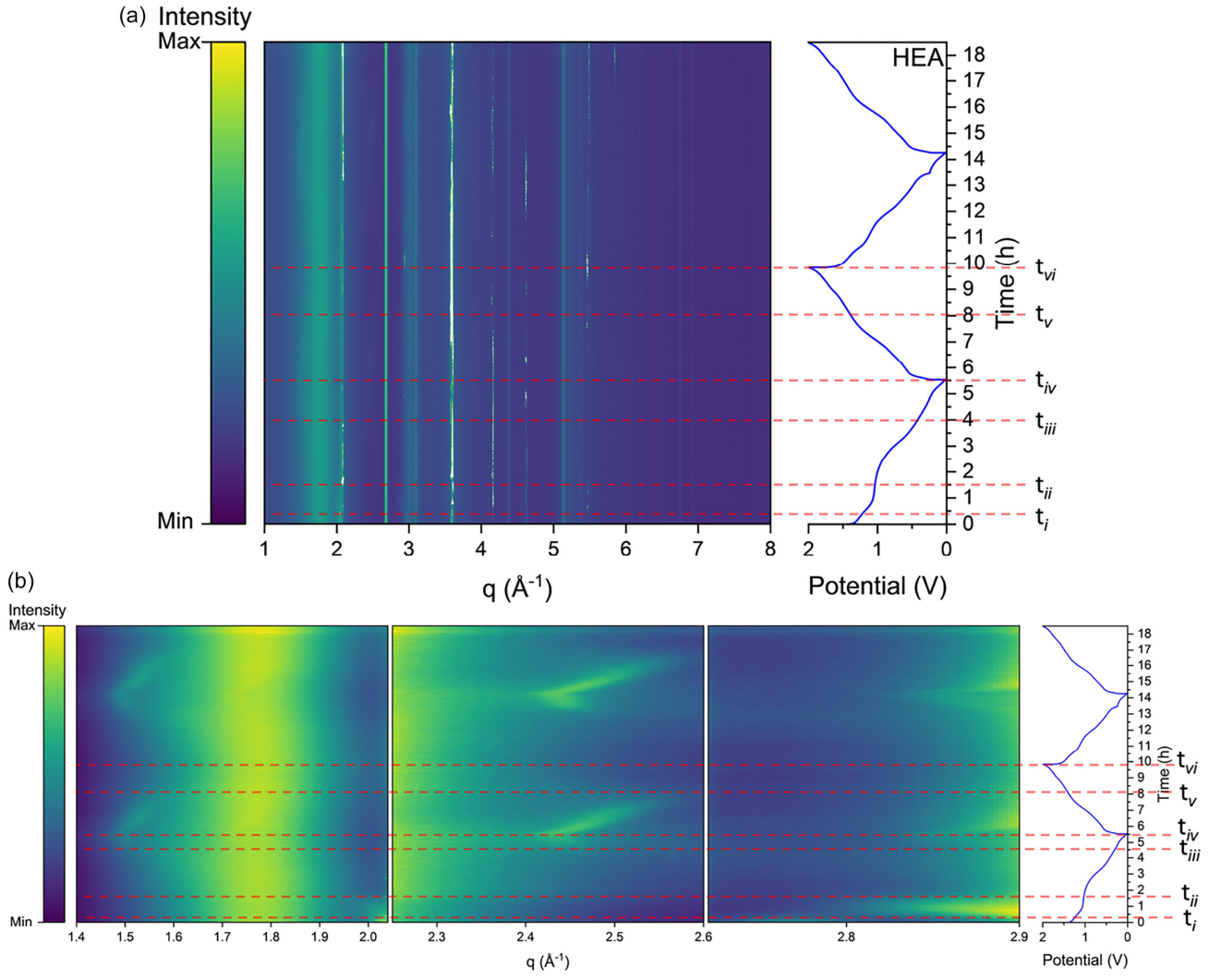


FIGURE 4 | Overall *operando* SXRD pattern of HEA (a) and specific regions of interest (b).

25666223, 2026, 11, Downloaded from https://chemistry-europe.onlinelibrary.wiley.com/doi/10.1002/batt.70521 by Chalmers University Of Technology, Wiley Online Library on [10/11/2026]. See the Terms and Conditions (https://onlinelibrary.wiley.com/terms-and-conditions) on Wiley Online Library for rules of use; OA articles are governed by the applicable Creative Commons License

provided as waterfall plots (Figures S10 and S11), which can provide a clearer overview of the evolution, albeit at reduced time resolution, which can lead to underrepresentation of some changes.

The evolution of the overall SXRD patterns of the HEA collected during the initial two cycles using the AMPIX cell (Figure 4a) and the magnified view of the regions of interest (Figure 4b) both indicate a similar phase separation as for MEA during the initial part of

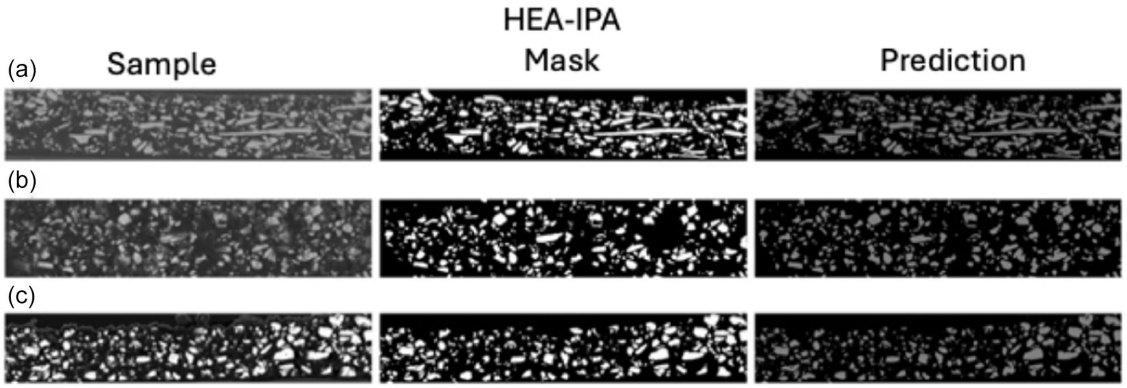


FIGURE 5 | SEM sample image, mask, and UNet model prediction for HEA-IPA electrodes; pristine (a), after 5 cycles (b), and after 30 cycles (c).

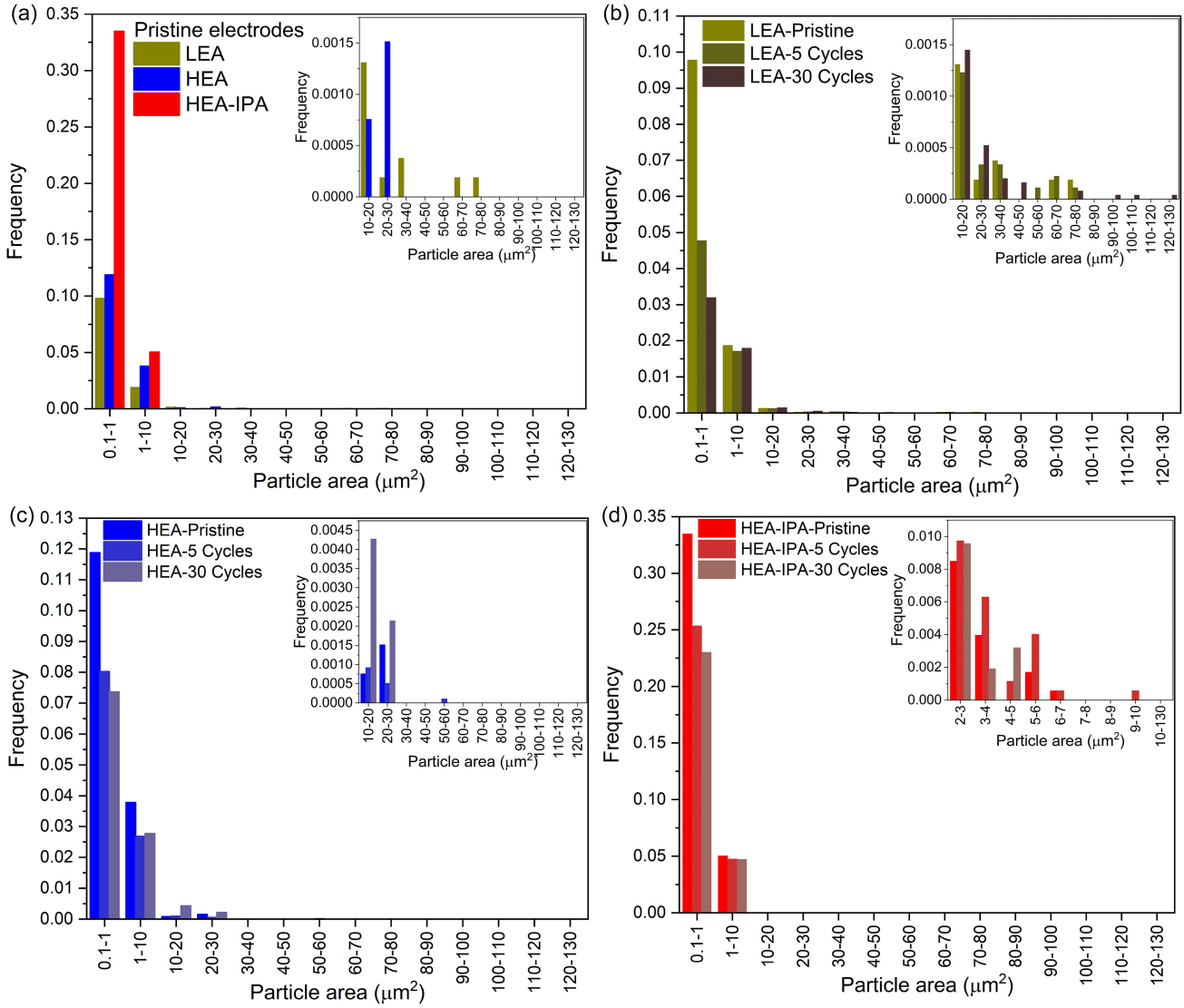


FIGURE 6 | Normalized particle size distributions of pristine LEA, HEA, and HEA-IPA electrodes (a), cycled LEA (b), HEA (c), and HEA-IPA (d) electrodes. Insets: The particle size distributions in the large particle area ranges.

25666223, 2026, 11, Downloaded from https://chemistry-europe.onlinelibrary.wiley.com/doi/10.1002/batt.70521 by Chalmers University Of Technology, Wiley Online Library on [10/11/2026]. See the Terms and Conditions (https://onlinelibrary.wiley.com/terms-and-conditions) on Wiley Online Library for rules of use; OA articles are governed by the applicable Creative Commons License

sodiation (between t_i and t_{ii}) and the formation of the "transformed" monoclinic $Na_2(TeSe_3)$ phase. The phase separation is observed more clearly using the hexagonal cell data (Figures S12 and S13), as the reflections originating from cell parts appear at different scattering vectors. During the major part of the sodiation (between t_{ii} and t_{iii}), however, no crystalline phase forms, suggesting that the sodium storage occurs through the formation of amorphous species (Figure 4b). This is possibly due to Sn atoms preventing the distribution of sodium homogeneously throughout the structure by not participating in the sodium storage due to their low alloying potential [47]. However, the exact role of Sn in modifying the reaction pathway in this complex system, other than preventing the formation of a crystalline structure, is not possible to determine through SXRD. As the sodiation continues below 0.5 V (between t_{iii} and t_{iv}), a cubic Na_xM structure, similar to that previously observed for MEA, forms and grows until HEA is fully sodiated (t_{iv}). Again, the formation of Na_xM is confirmed by comparing the ex situ SXRD pattern of fully sodiated FS HEA electrode and the ICSD XRD pattern of cubic Na_2Te (Figure S14). In addition, and in stark contrast to other ex situ XRD patterns, a broad feature is observed for $1.8 < q < 2.4\,Å^{-1}$, implying the formation of amorphous species (Figure S15).

During desodiation, the interplanar distance of the cubic structure decreases. This continues further beyond the original structure until the long-range order is completely lost (t_v). In stark contrast to MEA, the "transformed" structure is not reformed at the end of the cycle (t_{vi}), and rather amorphous or nanostructured species form in situ and become the electrochemically active component. Such an electrode "amorphization" was previously reported for Sb- and Sn-containing electrodes for both LIBs [48] and SIBs [17, 44, 49], and indeed also to improve the storage capacity [50, 51], in agreement with our present results. As for the MEA data, the structural evolution using AMPIX and hexagonal cell data is also provided as waterfall plots (Figures S16 and S17, respectively).

3.4 | Particle Size and Distribution

Cross-sectional SEM data and the CNN analysis allow the segmentation of the images and the identification of individual particles, providing particle size (area) information (Figures 5, S18, and S19).

The particle size distributions (Figure 6) and morphologies (Figure 7) reveal notable changes across the different electrodes and as function of cycling. In particular, HEA-IPA indeed has a much smaller initial particle size as compared to both LEA and HEA, and LEA has the widest distribution of particle sizes, with many particles $>50\,mm^2$, followed by HEA (Figure 6a). The LEA electrode (Figure 6b) demonstrates a shift towards larger particle sizes after cycling, with the largest particles observed

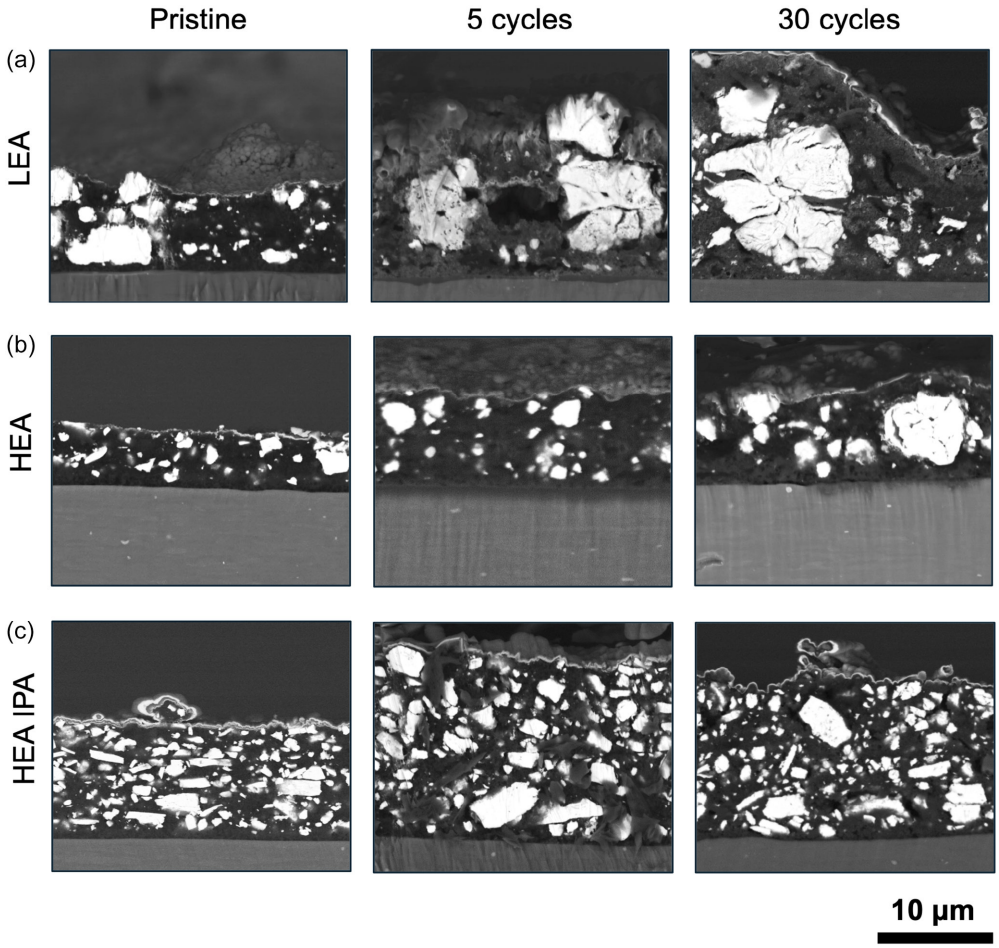


FIGURE 7 | SEM-BSE cross-sectional images showing the particle size and morphology for pristine and cycled (after 5 and 30 cycles) electrodes: LEA (a), HEA (b), and HEA-IPA (c).

25666223, 2026, 11, Downloaded from https://chemistry-europe.onlinelibrary.wiley.com/doi/10.1002/batt.70521 by Chalmers University Of Technology, Wiley Online Library on [10/11/2026]. See the Terms and Conditions (https://onlinelibrary.wiley.com/terms-and-conditions) on Wiley Online Library for rules of use; OA articles are governed by the applicable Creative Commons License

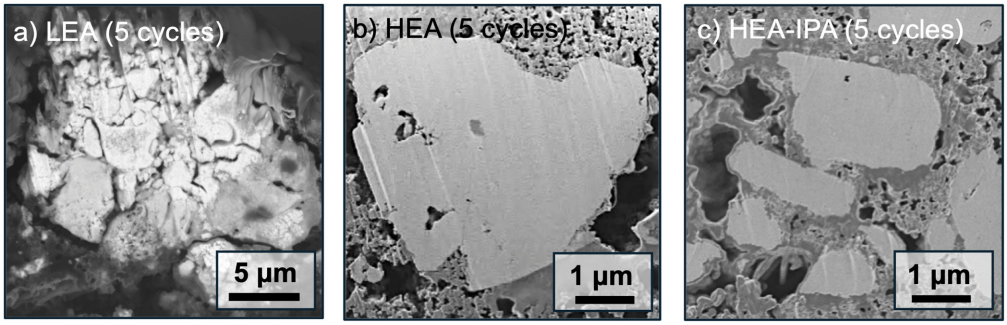


FIGURE 8 | SEM images (a: BSE and b–c: SE) showing the internal morphology of large particles after 5 cycles for LEA (a), HEA (b), and HEA-IPA (c).

after 30 cycles (Figures 6b and 7a). The HEA electrode also displays a shift towards larger particles after cycling. The small- to medium-size particles remain similar after 5 and 30 cycles, whereas the number of particles $>10\,\mu m^2$ increase after 30 cycles (Figures 6c and 7b). The HEA-IPA electrode displays a similar size distribution throughout cycling, with a slight shift towards larger particles after cycling (Figures 6d and 7c), with no particles $>10\,\mu m^2$ observed. Overall, this also clearly demonstrates the beneficial effect of BM with IPA, resulting in a more homogeneous size distribution, higher density, and overall smaller particle size (Figure 7b,c), ultimately reflected in the improved GC stability compared to HEA (Figure 2). These findings are in qualitative agreement with recent observations for a Si anode in a LIB cell, where larger particles result in less stable cycling due to electrode cracking [52].

The internal morphology of the larger particles after cycling demonstrates that in LEA, these exhibit substantial cracking after 5 cycles (as well as after 30 cycles) (Figure 8), indicating initiation of electrode pulverization. The HEA displays no similar cracking after 5 cycles but significant such after 30 cycles (Figure S23), while the HEA-IPA electrode remains intact throughout cycling, further substantiating the beneficial effect of smaller initial AM particle size on the cycling stability.

4 | Conclusions

By applying entropy-engineered alloy anodes, improved SIB cell cycling stability is obtained as compared to conventional alloys without any need for cumbersome compositing with conductive carbon. The stability observed is further enhanced by reducing the initial AM particle size by BM with IPA. The *operando* SXRD data reveal key information regarding the sodiation mechanism of both MEA- and HEA-based anodes, where the initial in situ structural transformation and the formation of amorphous structures at the fully sodiated state both contribute to the capacity, while the latter also keeps the structure intact, again highlighting the impact of entropy-engineering. However, as *operando* SXRD inherently is insensitive to amorphous materials, these are only tracked as either an increase in the background or as broad features in the normalized ex situ SXRD patterns. The analysis of particle morphology reveals trends in particle cracking consistent with the electrochemical performance, especially cycling stability, whereas the particle sizes connect to the capacities observed. Overall, these results show that HEAs are promising SIB alloy anodes, but also that much detail must be spent on exact monitoring and control of their phase evolution during (de)sodiation, which in addition becomes ever more important when/if up-scaling the synthesis.

Acknowledgments

The authors gratefully acknowledge financial support from the Knut and Alice Wallenberg Foundation (KAW) via the Wallenberg Initiative Materials Science for Sustainability (WISE), from the French National Research Agency via the project Labex STORE-EX (ANR-10-LABX-76-01), as well as from the Swedish Research Council's Distinguished Professor grant #2021-00613 on Next Generation Batteries to P.J. The authors also acknowledge MAX IV Laboratory for time on Beamline DanMAX under Proposal 2023023. Research conducted at MAX IV was supported by the Swedish Research Council under contract 2018-07152, the Swedish Governmental Agency for Innovation Systems under contract 2018-04969, and FORMAS under contract 2019-02496. DanMAX was funded by the NUFI grant no. 4059-00009B. The authors acknowledge Dr. Mads Ry Vogel Jørgensen for assistance during the beamtime. This work was performed in part at the Chalmers Materials Analysis Laboratory, CMAL. K.D. acknowledges Dr. Patricia Huijbers for valuable feedback and Dr. Ezio Zanghellini for technical assistance.

Funding

This work was funded by the Knut and Alice Wallenberg Foundation (KAW) via the Wallenberg Initiative Materials Science for Sustainability (WISE); Agence Nationale de la Recherche (ANR-10-LABX-76-01); Vetenskapsrådet (2021-00613 and 2018-07152); VINNOVA (2018-04969); and Svenska Forskningsrådet Formas (2019-02496).

Conflicts of Interest

The authors declare no conflicts of interest.

Data Availability Statement

The data that support the findings of this study are available from the corresponding author upon reasonable request.

References

1. S. Wickerts, R. Arvidsson, A. Nordelöf, and M. Svanström, "Prospective Life Cycle Assessment of Sodium-Ion Batteries Made From Abundant Elements," *Journal of Industrial Ecology* 29, no. 1 (2024): 116–129, https://doi.org/10.1111/jiec.13452.

2. S. Ma, W. Yan, Y. Dong et al., "Recent Advances in Carbon-Based Anodes for High-Performance Sodium-Ion Batteries: Mechanism, Modification

25666223, 2026, 11, Downloaded from https://chemistry-europe.onlinelibrary.wiley.com/doi/10.1002/batt.70521 by Chalmers University Of Technology, Wiley Online Library on [10/11/2026]. See the Terms and Conditions (https://onlinelibrary.wiley.com/terms-and-conditions) on Wiley Online Library for rules of use; OA articles are governed by the applicable Creative Commons License

and Characterizations," *Materials Today* 75 (2024): 334–358, https://doi.org/10.1016/j.mattod.2024.04.007.

3. G. Chang, Y. Zhao, L. Dong, et al., "A Review of Phosphorus and Phosphides as Anode Materials for Advanced Sodium-Ion Batteries," *Journal of Materials Chemistry A* 8 (2020): 4996–5048, https://doi.org/10.1039/C9TA12169B.

4. A. Fereydooni, C. Yue, and Y. Chao, "A Brief Overview of Silicon Nanoparticles as Anode Material: A Transition From Lithium-Ion to Sodium-Ion Batteries," *Small* 20 (2024): 1–17, https://doi.org/10.1002/smll.v20.17.

5. L. C. Loaiza, L. Monconduit, and V. Seznec, "Si and Ge-Based Anode Materials for Li-, Na-, and K-Ion Batteries: A Perspective From Structure to Electrochemical Mechanism," *Small* 16 (2020): 1–29, https://doi.org/10.1002/smll.v16.5.

6. S. M. Zheng, Y. R. Tian, Y. X. Liu, et al., "Alloy Anodes for Sodium-Ion Batteries," *Rare Metals* 40 (2021): 272–289, https://doi.org/10.1007/s12598-020-01605-z.

7. Y. Jiang, Z. Zhang, H. Liao, et al., "Progress and Prospect of Bimetallic Oxides for Sodium-Ion Batteries: Synthesis, Mechanism, and Optimization Strategy," *ACS Nano* 18 (2024): 7796–7824, https://doi.org/10.1021/acsnano.4c00613.

8. S. Dai, L. Wang,M. Cao, Z. Zhong, Y. Shen, and M. Wang, "Design Strategies in Metal Chalcogenides Anode Materials for High-Performance Sodium-Ion Battery," *Materials Today Energy* 12 (2019): 114–128, https://doi.org/10.1016/j.mtener.2018.12.011.

9. N. Tapia-Ruiz, A. R. Armstrong, H. Alptekin, et al., "2021 Roadmap for Sodium-Ion Batteries," *Journal of Physics: Energy* 3 (2021): 031503, https://doi.org/10.1088/2515-7655/ac01ef.

10. J. Cui, S. Yao, and J. K. Kim, "Recent Progress in Rational Design of Anode Materials for High-Performance Na-Ion Batteries," *Energy Storage Materials* 7 (2017): 64–114, https://doi.org/10.1016/j.ensm.2016.12.005.

11. M. Lao, Y. Zhang, W. Luo, Q. Yan, W. Sun, and S. X. Dou, "Alloy-Based Anode Materials Toward Advanced Sodium-Ion Batteries," *Advanced Materials* 29 (2017): 1–23, https://doi.org/10.1002/adma.v29.48.

12. C. H. Lim, T.-Y. Huang, P.-S. Shao, et al., "Experimental Study on Sodiation of Amorphous Silicon for Use as Sodium-Ion Battery Anode," *Electrochimica Acta* 211 (2016): 265–272, https://doi.org/10.1016/j.electacta.2016.06.031.

13. Z. Zhang, X. Zhao, and J. Li, "SnSe/Carbon Nanocomposite Synthesized by High Energy Ball Milling as an Anode Material for Sodium-Ion and Lithium-Ion Batteries," *Electrochimica Acta* 176 (2015): 1296–1301, https://doi.org/10.1016/j.electacta.2015.07.140.

14. S. Guo and C. T. Liu, "Phase Stability in High Entropy Alloys: Formation of Solid-Solution Phase or Amorphous Phase," *Progress in Natural Science: Materials International* 21 (2011): 433–446, https://doi.org/10.1016/S1002-0071(12)60080-X.

15. S. Yuan, J. Wei, Z. Ma, et al., "High-Entropy Materials Chemistry for Electrochemical Energy Storage," *Chemical Reviews* 126, no. 3 (2026), 2218–2282, https://doi.org/10.1021/acs.chemrev.5c00783.

16. B. Ouyang and Y. Zeng, "The Rise of High-Entropy Battery Materials," *Nature Communications* 15 (2024): 1–5, https://doi.org/10.1038/s41467-024-45309-9.

17. A. Darwiche, M. T. Sougrati, B. Fraisse, L. Stievano, and L. Monconduit, "Facile Synthesis and Long Cycle Life of SnSb as Negative Electrode Material for Na-Ion Batteries," *Electrochemistry Communications* 32 (2013): 18–21, https://doi.org/10.1016/j.elecom.2013.03.029.

18. H. Gao, J. Niu, C. Zhang, Z. Peng, and Z. Zhang, "A Dealloying Synthetic Strategy for Nanoporous Bismuth-Antimony Anodes for Sodium Ion Batteries," *ACS Nano* 12 (2018): 3568–3577, https://doi.org/10.1021/acsnano.8b00643.

19. M. R. Panda, A. Raj K, A. Ghosh et al., "Blocks of Molybdenum Ditelluride: A High Rate Anode for Sodium-Ion Battery and Full Cell Prototype Study," *Nano Energy* 64 (2019): 103951, https://doi.org/10.1016/j.nanoen.2019.103951.

20. B. Farbod, K. Cui, W. P. Kalisvaart, et al., "Anodes for Sodium Ion Batteries Based on Tin-Germanium-Antimony Alloys," *ACS Nano* 8 (2014): 4415–4429, https://doi.org/10.1021/nn4063598.

21. E. Edison, S. Sreejith, H. Ren, C. T. Lim, and S. Madhavi, "Microstructurally Engineered Nanocrystalline Fe-Sn-Sb Anodes: Towards Stable High Energy Density Sodium-Ion Batteries," *Journal of Materials Chemistry A* 7 (2019): 14145–14152, https://doi.org/10.1039/C9TA01158G.

22. D. Sun, G. Zhang, D. Li, S. Liu, X. Jia, and J. Zhou, "A Layered Bi2Te3 Nanoplates/Graphene Composite With High Gravimetric and Volumetric Performance for Na-Ion Storage," *Sustainable Energy & Fuels* 3 (2019): 3163–3171, https://doi.org/10.1039/C9SE00544G.

23. M. W. Orzech, F. Mazzali, J. D. McGettrick, et al., "Synergic Effect of Bi, Sb and Te for the Increased Stability of Bulk Alloying Anodes for Sodium-Ion Batteries," *Journal of Materials Chemistry A* 5 (2017): 23198–23208, https://doi.org/10.1039/C7TA07648G.

24. S. Alvi, A. P. Black, I. Jozami, C. Escudero, F. Akhtar, and P. Johansson, "Entropy Stabilized Medium High Entropy Alloy Anodes for Lithium-Ion Batteries," *Batteries & Supercaps* 7, no. 5 (2024): e202300585, https://doi.org/10.1002/batt.202300585.

25. S. Alvi, A. Fazi, D. Weber, D. Hedman, and K. Choudhary, "EES Batteries Batteries : Entropy and Nano-Level Heterogeneity e Ff Ects," *EES Batteries* 2, no. 3 (2026): 1003–1011, https://doi.org/10.1039/d6eb00032k.

26. D. Bresser, S. Passerini, and B. Scrosati, "Environmental Science Alloying and Conversion for Lithium-Ion Anodes †," *Energy & Environmental Science* 9 (2016): 3348–3367, https://doi.org/10.1039/C6EE02346K.

27. L. Fang, N. Bahlawane, W. Sun, et al., "Conversion-Alloying Anode Materials for Sodium Ion Batteries," *Small* 17 (2021): 1–38, https://doi.org/10.1002/smll.202101137.

28. M. Wood, X. Gao, R. Shi, et al., "Exploring the Relationship Between Solvent-Assisted Ball Milling, Particle Size, and Sintering Temperature in Garnet-Type Solid Electrolytes," *Journal of Power Sources* 484 (2021): 229252, https://doi.org/10.1016/j.jpowsour.2020.229252.

29. C. A. Schneider, W. S. Rasband, and K. W. Eliceiri, "NIH Image to ImageJ: 25 Years of Image Analysis," *Nature Methods* 9 (2012): 671–675, https://doi.org/10.1038/nmeth.2089.

30. K. Choudhary, I. O. Santos Mendoza, A. Nadeina, et al., "Operando X-Ray Diffraction in Transmission Geometry « at Home » From Tape Casted Electrodes to All-Solid-State Battery," *Journal of Power Sources* 553 (2023): 232270, https://doi.org/10.1016/j.jpowsour.2022.232270.

31. O. J. Borkiewicz, B. Shyam, K. M. Wiaderek, C. Kurtz, P. J. Chupas, and K. W. Chapman, "The AMPIX Electrochemical Cell: A Versatile Apparatus for In Situ X-Ray Scattering and Spectroscopic Measurements," *Journal of Applied Crystallography* 45 (2012): 1261–1269, https://doi.org/10.1107/S0021889812042720.

32. S. Ioffe and C. Szegedy, "Batch Normalization: Accelerating Deep Network Training by Reducing Internal Covariate Shift," in 32nd Int. Conf. Mach. Learn. ICML 2015, 1 (2015): 448–456.

33. A. F. Agarap, "Deep Learning using Rectified Linear Units (ReLU)," arXiv:1803.08375 (2019). https://doi.org/10.48550/arXiv.1803.08375.

34. Z. Zhang, "Improved Adam Optimizer for Deep Neural Networks," in 2018 IEEE/ACM 26th Int. Symp. Qual. Serv. IWQoS 2018 (2018), 1–2, https://doi.org/10.1109/IWQoS.2018.8624183.

35. Z. Zhang and M. R. Sabuncu, "Generalized Cross Entropy Loss for Training Deep Neural Networks With Noisy Labels," *Advances in Neural Information Processing Systems* 2018 (Dec 2018): 8778–8788.

36. S. Cao, M. H. Tahmasebi, S. Gracious, J. C. Bennett, and M. N. Obrovac, "Preparation of Low Surface Area Si-Alloy Anodes for Li-Ion Cells by Ball Milling," *Journal of the Electrochemical Society* 169 (2022): 060540.

25666223, 2026, 11, Downloaded from https://chemistry-europe.onlinelibrary.wiley.com/doi/10.1002/batt.70521 by Chalmers University Of Technology, Wiley Online Library on [10/11/2026]. See the Terms and Conditions (https://onlinelibrary.wiley.com/terms-and-conditions) on Wiley Online Library for rules of use; OA articles are governed by the applicable Creative Commons License

37. D. Li, J. Zhou, X. Chen, and H. Song, "Graphene-Loaded Bi2Se3: A Conversion-Alloying-Type Anode Material for Ultrafast Gravimetric and Volumetric Na Storage," *ACS Applied Materials & Interfaces* 10 (2018): 30379–30387, https://doi.org/10.1021/acsami.8b09538.

38. A. Darwiche, M. Toiron, M. T. Sougrati, B. Fraisse, L. Stievano, and L. Monconduit, "Performance and Mechanism of FeSb2 as Negative Electrode for Na-Ion Batteries," *Journal of Power Sources* 280 (2015): 588–592, https://doi.org/10.1016/j.jpowsour.2015.01.138.

39. H. Xie, W. P. Kalisvaart, B. C. Olsen, E. J. Luber, D. Mitlin, and J. M. Buriak, "Sn-Bi-Sb Alloys as Anode Materials for Sodium Ion Batteries," *Journal of Materials Chemistry A* 5 (2017): 9661–9670, https://doi.org/10.1039/C7TA01443K.

40. C. Wang, D. Du, M. Song, Y. Wang, and F. Li, "A High-Power $Na_3V_2(PO_4)_3$-Bi Sodium-Ion Full Battery in a Wide Temperature Range," *Advanced Energy Materials* 2 (2019): 2–8, https://doi.org/10.1002/aenm.201900022.

41. Y. Kravets, Y. Sun, H. Wang, and P. Adelhelm, "Role of Silicon as Structural Stabilizer and Redox-Active Element in Multicomponent (Sn, Sb, Fe, Si) Alloy Electrodes for Na-Ion Batteries," *Batteries & Supercaps* 8, no. 6 (2025): 1–10, https://doi.org/10.1002/batt.v8.6, 202400690.

42. J. Zhao, J. Yue, S. Gao, and T. Li, "Synergistic Multi-Element Strategy Enables SnSbMnBiTe High-Entropy Alloy Anode for Stable and Fast Sodium Storage," *ACS Sustainable Chemistry & Engineering* 13, no. 28 (2025): 11143–11152, https://doi.org/10.1021/acssuschemeng.5c04513.

43. Y. Zhang, J. Xing, M. Chen, and Q. Jin, "High-Entropy Metal Diselenides Propels Polyselenides Immobilization for High Performance Sodium Storage," *Chemical Engineering Journal* 479 (2024): 147709, https://doi.org/10.1016/j.cej.2023.147709.

44. A. Darwiche, C. Marino, M. T. Sougrati, B. Fraisse, L. Stievano, and L. Monconduit, "Better Cycling Performances of Bulk Sb in Na-Ion Batteries Compared to Li-Ion Systems: An Unexpected Electrochemical Mechanism," *Journal of the American Chemical Society* 134 (2012): 20805–20811, https://doi.org/10.1021/ja310347x.

45. M. E. Leonova, I. K. Bdikin, S. A. Kulinich, and O. K. Gulish, "High-Pressure Phase Transition of Hexagonal Alkali Pnictides," *Inorganic Materials* 39 (2003): 266–270, https://doi.org/10.1023/A:1022629709143.

46. M. Saubanère, M. Ben Yahia, F. Lemoigno, and M.-L. Doublet, "Influence of Polymorphism on the Electrochemical Behavior of M Sb Negative Electrodes in Li/Na Batteries," *Journal of Power Sources* 280 (2015): 695–702, https://doi.org/10.1016/j.jpowsour.2015.01.093.

47. S. Kim, W. Tang, D. J. Lee, et al., "Tin Anode for High-Energy-Density Na-Ion Batteries," *Journal of The Electrochemical Society*, 172, no. 10 (2025): 100541, https://doi.org/10.1149/1945-7111/ae0fc4.

48. C. Marino, B. Fraisse, M. Womes, C. Villevieille, L. Monconduit, and L. Stievano, "At the Heart of a Conversion Reaction: An Operando X-Ray Absorption Spectroscopy Investigation of NiSb2, a Negative Electrode Material for Li-Ion Batteries," *Journal of Physical Chemistry C* 118 (2014): 27772–27780, https://doi.org/10.1021/jp5097579.

49. P. K. Allan, J. M. Griffin, A. Darwiche, et al., "Tracking Sodium-Antimonide Phase Transformations in Sodium-Ion Anodes: Insights From Operando Pair Distribution Function Analysis and Solid-State NMR Spectroscopy," *Journal of the American Chemical Society* 138 (2016): 2352–2365, https://doi.org/10.1021/jacs.5b13273.

50. S. Abdul Ahad, S. Kilian, M. Zubair, et al., "Amorphization Driven Na-Alloying in SixGe1−xalloy Nanowires for Na-Ion Batteries," *Journal of Materials Chemistry A*9 (2021): 20626–20634, https://doi.org/10.1039/D1TA03741B.

51. A. Kohandehghan, K. Cui, M. Kupsta, et al., "Activation With Li Enables Facile Sodium Storage in Germanium," *Nano Letters* 14 (2014): 5873–5882, https://doi.org/10.1021/nl502812x.

52. F. Wu, Y. Dong, Y. Su, et al., "Benchmarking the Effect of Particle Size on Silicon Anode Materials for Lithium-Ion Batteries," *Small* 19 (2023): 2301301, https://doi.org/10.1002/smll.202301301.

Supporting Information

Additional supporting information can be found online in the Supporting Information section.

25666223, 2026, 11, Downloaded from https://chemistry-europe.onlinelibrary.wiley.com/doi/10.1002/batt.70521 by Chalmers University Of Technology, Wiley Online Library on [10/11/2026]. See the Terms and Conditions (https://onlinelibrary.wiley.com/terms-and-conditions) on Wiley Online Library for rules of use; OA articles are governed by the applicable Creative Commons License